

Article

Aerodynamic Heating Ground Simulation of Hypersonic Vehicles Based on Model-Free Control Using Super Twisting Nonlinear Fractional Order Sliding Mode

Xiaodong Lv ^{1,2}, Guangming Zhang ^{1,*} , Mingxiang Zhu ¹, Zhihan Shi ¹, Zhiqing Bai ¹ and Igor V. Alexandrov ²

¹ College of Electrical Engineering and Control Science, Nanjing Tech University, Nanjing 211899, China; lxd@njtech.edu.cn (X.L.); mxzhu@njtech.edu.cn (M.Z.); szh@njtech.edu.cn (Z.S.); baizhiqing1024@njtech.edu.cn (Z.B.)

² Institute of Physics of Advanced Materials, Ufa State Aviation Technical University, 12 K. Marx St., 450000 Ufa, Russia; igorvalexandrov@yandex.ru

* Correspondence: zgm@njtech.edu.cn

Abstract: In this article, a model-free control (MFC) using super twisting nonlinear fractional order sliding mode for aerodynamic heating ground simulation of hypersonic vehicles (AHGSHV) is proposed. Firstly, the mathematical model of AHGSHV is built up. To reduce order and simplify the dynamic model of AHGSHV, an ultra-local model of MFC is taken into consideration. Then, time delay estimation can be used to estimate systematic uncertainties and external unknown disturbances. On the basis of the original fractional order sliding mode surface, the nonlinear function *fal* is introduced to design the nonlinear fractional order sliding mode surface, which can guarantee stability, increase convergence rate, and reduce static error and saturation error. In addition, the super twisting reaching law is used to improve the control performance of the reaching phase, resulting from the existence of sign function in the integral term, and it can effectively reduce the high-frequency chattering. Moreover, the Lyapunov function is used to prove the stability of the whole system. Finally, several numerical simulations show that the designed controller has more advantages than others.

Keywords: aerodynamic heating ground simulation; hypersonic vehicles; model-free control; nonlinear fractional order sliding mode

MSC: 93B05; 93B18; 93B52



Citation: Lv, X.; Zhang, G.; Zhu, M.; Shi, Z.; Bai, Z.; Alexandrov, I.V. Aerodynamic Heating Ground Simulation of Hypersonic Vehicles Based on Model-Free Control Using Super Twisting Nonlinear Fractional Order Sliding Mode. *Mathematics* **2022**, *10*, 1664. <https://doi.org/10.3390/math10101664>

Academic Editors: Yiming Chen, Aimin Yang, Jiaquan Xie and Yanqiao Wei

Received: 6 April 2022

Accepted: 11 May 2022

Published: 12 May 2022

Publisher's Note: MDPI stays neutral with regard to jurisdictional claims in published maps and institutional affiliations.



Copyright: © 2022 by the authors. Licensee MDPI, Basel, Switzerland. This article is an open access article distributed under the terms and conditions of the Creative Commons Attribution (CC BY) license (<https://creativecommons.org/licenses/by/4.0/>).

1. Introduction

During a high-speed flight, the surface of hypersonic vehicles (HV) [1] moves relative to the airstream, which generates a lot of heat, causing the rapidly rising surface temperature of HV. This phenomenon is known as aerodynamic heating [2]. Excessive surface temperature not only affects the normal operation of HV, but also poses a threat to structural safety of the air frame and stability of internal electronic equipment. Therefore, it is necessary to simulate the thermal environment of HV during high-speed flight for thermal protection systems (TPS) [3].

There are two main kinds of aerodynamic heating ground simulation of hypersonic vehicles (AHGSHV): convection heating [4] and radiation heating [5]. The wind tunnel [6] is a typical convection heating facility, which is mainly realized by the high-speed relative motion between the airstream medium and the test piece. Because of too high flight Mach number, the complex thermal environment cannot be accurately simulated by the wind tunnel. It just generally provides the limited data parameters for the design of aerodynamic thermal shape structure, which is not suitable for the research of structural characteristics. By contrast, radiation heating is based on the thermal effect of resistance to radiate heat energy outward. The thermal radiation elements include chromium-nickel [7],

silicon-carbon [8], graphite [9], and quartz lamps. Compared with other thermal radiation elements, quartz lamp heaters [10] have some excellent properties, such as small size, large power, small thermal inertia, and safe operation. Some researchers focus on studying quartz lamp heaters. In [11], the power optimization of non-uniform aerodynamic heating based on a quartz lamp array is analyzed. In [12], a numerical method based on a finite volume method for a quartz lamp heating system is used for thermal testing. In [13], a new type of quartz lamp heater with a high heating rate is up to 1500 °C. Based on the above research, we establish a quartz lamp heaters platform for AHGSHV. In Figure 1, there are four parts in the control system for AHGSHV: a control center, a power regulator, quartz lamp heaters, and temperature sensor. The control center can facilitate feedback information exchanges between reference temperature trajectory and actual output temperature value, associated with analog-to-digital conversion. The transistor, named silicon-controlled rectifier (SCR), is a power regulator by adjusting the input power of quartz lamp heaters. Quartz lamp heaters obtain different power values to have a controlled thermal radiation ability and provide a variable thermal environment for untested HV. The temperature sensor, K_Thermocouple, has a high-temperature detection ability and exchanges feedback temperature values of the thermal environment to the control center.

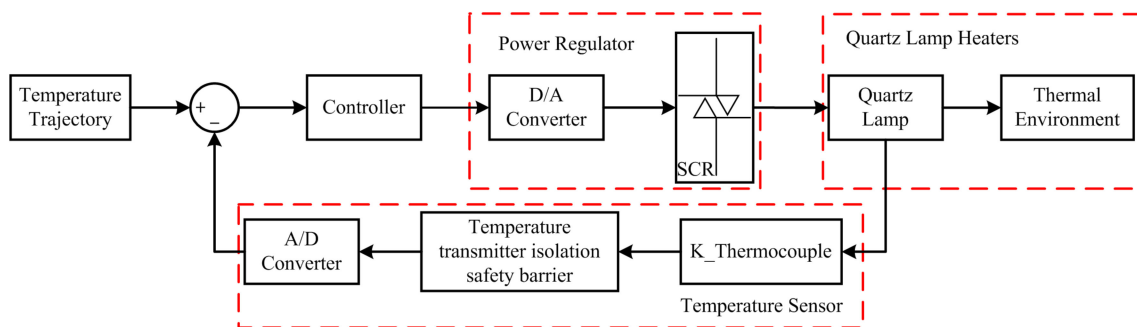


Figure 1. The flow chart of the control system for AHGSHV [14].

The quartz lamp heaters platform, named AHGSHV system, is a nonlinear system with large thermal inertia and time delay. For such a complex system, the traditional linear controller cannot meet the requirements of accurate tracking. Therefore, a number of advanced control theories have been applied widely for nonlinear objects, such as fuzzy logic control [15], neural network control [16], adaptive control [17], and sliding mode control (SMC) [18]. In [15], an interval type-2 fuzzy logic control combined with the Takagi-Sugeno-Kang (TSK) technique is compared with a type-1 TSK fuzzy logic control and a traditional proportional-derivative (PD) for an inverted pendulum and cart model. In [16], a reachability analysis approach of neural network with Bernstein polynomials is proposed. In contrast with Sherlock and Verisig, the proposed scheme can present comparable or even better approximation performance. Among these control approaches, fuzzy logic control is independent of the accurate systematic model and only requires input gain and output measurement, which has certain robustness to fault tolerance; neural network control can approximate some nonlinear systems. However, both of them need a large amount of rulemaking and parameter tuning, which may reduce the likelihood and effectiveness of implementation.

In order to solve the problems mentioned above, model-free control (MFC) [19] is taken into consideration for the AHGSHV system, which generally utilizes an ultra-local model to replace the complex mathematical model of the controlled object, rather than relying on the system dynamic model heavily. MFC usually has two parts: a closed-loop controller and a real-time compensator. An intelligent proportional-integral-derivative controller (IPID) is usually chosen as the closed-loop controller. In [20], an IPI sliding mode control is developed for direct power control of the doubly fed induction generator wind turbine systems in terms of stochastic wind and parameter variations. In [21], an IPD neural network control based on time-delay estimation is applied to five DOFs lower

limb exoskeleton. However, the linear superposition of PID can cause the contradiction from rapidity to overshoot. Hence, SMC can be regarded as the closed-loop controller to replace PID.

Sliding mode control (SMC) is one of the most influential methods and has the characteristics of fast response, the insensitivity to dynamic uncertainties and disturbances. Because of these advantages, SMC is widely used in a variety of controlled objects. In order to enhance further control accuracy and convergence speed, many controllers combined with SMC are put forward, such as terminal SMC, adaptive SMC, fuzzy SMC, and neural networks SMC. In [22], a terminal SMC is proposed to control the position and attitude of the quadrotor aircraft. In [23], a new adaptive sliding mode fault-tolerant control for event-triggered dynamic systems is designed. In [24], a fuzzy SMC is proposed and applied for the wind power generation system to achieve optimal power tracking by adjusting the speed of the generator. In [25], for a class of piezoelectric actuated systems, a new online neural-network-based SMC scheme is developed to obtain robust adaptive precision motions. In [26], a sliding surface without a reaching phase is presented for uncertain fractional-order systems. Two different methods, integer reaching law and fractional reaching law, are applied to keep the trajectories on the initial sliding surface. At the same time, these schemes are all integral order in lack extra degrees of freedom from integrator and differentiator and it may lead to more chattering [27]. So, the fractional theory should be combined with SMC.

The linear fractional order SMC (LFOSMC) is widely used in some controlled objects, such as permanent magnet synchronous motor [28], robotic manipulator [29], fully-actuated, and under-actuated nonlinear systems [30]. In [31], this paper proposes a fractional order $PI^{\lambda}D$ sliding mode with a neural network for hypersonic vehicles. In [30], an interval type-2 fuzzy fractional order super twisting algorithm (IT2FFOSTA) is employed for fully-actuated and under-actuated nonlinear systems. However, the structure of LFOSMC is simple, and the tuning parameters are only the coefficients of proportional, integral, and differential terms [32,33]. Then, a nonlinear FOSMC (NFOSMC) is designed by referring to a nonlinear function *fal* [28,34], which has the characteristics of fast convergence and reduces steady-state error and saturate error. NFOSMC contains the advantages of LFOSMC and the nonlinear function *fal* [35]. In addition, combined with reaching the law of super twisting algorithm, the sign function appears in the integral term, which can effectively reduce the high-frequency chattering [36]. Based on NFOSMC and super twisting algorithm, a super twisting nonlinear fractional order sliding mode control (STNFOSMC) is proposed for the AHGSHV system.

On the other hand, because of some uncertainties and external disturbances of the AHGSHV system, it cannot guarantee accurate convergence. In terms of a real-time compensator, it can use an estimation technique to observe all unknown terms and disturbances. Time delay estimation (TDE) [37] can effectively obtain the unknown lumped system dynamics owing to time-delayed signals from inputs and outputs, instead of changing controller gains or system parameters. TDE, as an estimation technique, provides a model-free nature because of its simple structure and easy use. So, in this paper, a STNFOSMCTDE based on MFC is designed for the AHGSHV system.

The main contributions of this paper are listed:

1. Based on the thermal radiation characteristics of quartz lamp heaters, an aerodynamic heating ground simulation, named AHGSHV system, is established and we propose a mathematical model of the AHGSHV system by energy conservation.
2. Due to high nonlinearities and strong couplings from trigonometric functions and high order terms, a STNFOSMCTDE strategy is obtained to guarantee fast response, strong robustness, and accurate tracking. In the frame of model-free control, a STNFOSMC, as a closed-loop controller and a TDE, as lumped uncertainties estimator is integrated into an ultra-local model.
3. The nonlinear function *fal* is introduced into a fractional order sliding mode surface for the goal of reducing steady-state error and saturate error.

4. A wing of HV is chosen as the calculated object and the reference temperature trajectory in time sequence is got by flow simulation of SolidWorks 2018.
5. Through comparative simulations, simulation results are used to verify that the STNFOSMCTDE controller is superior to the compared controller in terms of rapidity, overshoot, and anti-interference ability.

In this paper, a conception of aerodynamic heating ground reproduction with quartz lamp heaters is presented and we pay more attention to the theoretical analyses of the AHGSHV system and its control method. However, we ignore that not only is the heating environment considered, but also vibration, sound, and their coupling analyses are needed, during a real hypersonic fighting environment.

The structure of this paper is as follows. In Section 2, the model of the AHGSHV system is given in detail. In Section 3, the design of the controller is discussed and the proof of Lyapunov stability is given. In Sections 4 and 5, comparison and analysis of the simulation results are to verify the reliability of the proposed method. Finally, the conclusions of the paper are presented in Section 6.

2. AHGSHV System Modeling

In this section, the flow chart of the AHGSHV system is introduced, and the mathematical model of the AHGSHV system is established, which is composed of two parts: electrical energy and thermal radiation energy. As is shown in Figure 2, the whole system mainly includes three parts: aerothermal data acquisition, control system, and experimental feedback. In the first part, the parameters of HV's three-dimensional model, material, flight environment, flight altitude, flight speed, angle of attack and so on, should be predetermined. Then, the thermal environment of HV is simulated through the hydrodynamics simulation platform (SolidWorks 2018 Flow Simulation), and the numerical analysis results are as the expected output value of the AHGSHV system, which are used to compare with the actual output value in the control system. In the second part, the filament type of quartz lamp heaters should be confirmed as well. According to the selected parameters, the mathematical model of quartz lamp heaters is established, and the controller with good robust performance is designed to track the expected output value. In the third part, the TPS of HV is tested and analyze whether the selected materials and designed structures can withstand the thermal environment.

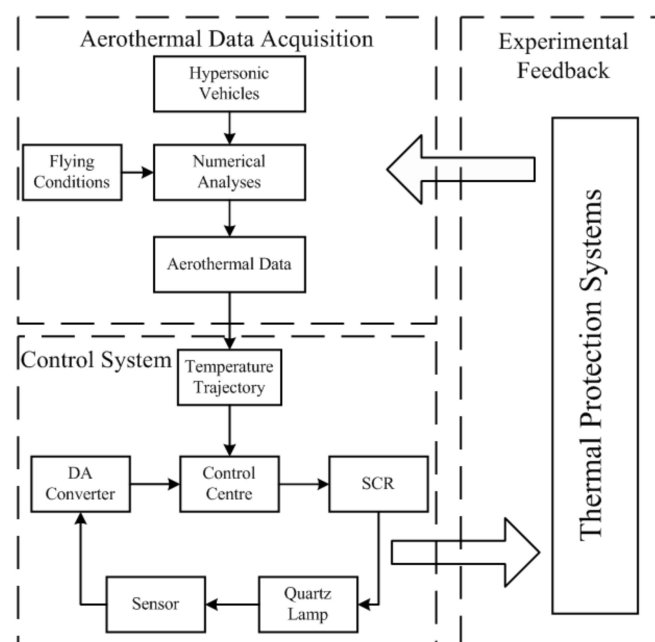


Figure 2. The flow chart of the AHGSHV system.

2.1. Electrical Energy

The AHGSHV system is based on quartz lamp heaters. By adjusting their input power, the AHGSHV system can possess a controlled thermal radiation ability.

The electrical energy as the total input $W(t) \in \mathbb{R}^+$ of AHGSHV system (J) can be calculated:

$$W(t) = P(t) * t \tag{1}$$

where, $P(t) \in \mathbb{R}^+$ is the electrical power (W) and $t \in \mathbb{R}^+$ is the heating time (S) of quartz lamp heaters.

Concretely, on the basis of an SCR adjusting voltage circuit, $P(t)$ can be described:

$$P(t) = \frac{U^2(t)}{R} \tag{2}$$

$$U(t) = \sqrt{\frac{1}{\pi} \int_{\alpha(t)}^{\pi} [\sqrt{2}U_1 \sin(\omega t)]^2 d(\omega t)} = U_1 \sqrt{\frac{\sin[2\alpha(t)]}{2\pi} + \frac{\pi - \alpha(t)}{\pi}} \tag{3}$$

where, $U(t) \in \mathbb{R}^+$ is the output voltage (V) of quartz lamp heaters; $R \in \mathbb{R}^+$ is the total resistance of the quartz lamp filament; $U_1 \in \mathbb{R}^+$ is the voltage (V) of source; $\omega t \in [0 \ \pi]$ is phase position (rad); $\alpha(t) \in [0 \ \pi]$ is the conduction angle of the thyristor (rad).

Then, substituting (2) and (3) to (1), $W(t)$ can be obtained:

$$W(t) = P(t) * t = \frac{U_1^2}{R} \left\{ \frac{\sin[2\alpha(t)]}{2\pi} + \frac{\pi - \alpha(t)}{\pi} \right\} t \tag{4}$$

2.2. Thermal Radiation Energy

The sum of thermal radiation energy generated by quartz lamp heaters [38] may consist of four ones: internal energy of the constant volume heat capacity; heating losses from heating conduction and heating radiation; viscous flowing energy dissipation; pressure energy from expansion or compression.

In macroscopic size, the shear strength of the quartz lamp is weak, so the effect of viscous dissipation on heat flow is slight, and the volume ratio of thermal expansion is small. Hence, assuming that the whole system satisfies the following conditions: (1) heat generated by viscous dissipation of specimens is not considered; (2) thermal expansion during heat transfer in AHGSHV is ignored, $Q(t) \in \mathbb{R}^+$ (J) can be further got:

$$Q(t) = cm[T_1(t) - T_0] + A \left\{ \beta[T_1(t) - T_0] + \lambda[T_1(t) - T_0] + \varepsilon\sigma FT_1^4(t)t \right\} \tag{5}$$

where, the first term on the right represents the internal energy; $c \in \mathbb{R}^+$ and $m \in \mathbb{R}^+$ are the specific heat capacity (J/kg·K) and the mass (kg) of the filament, respectively. $T_1(t) \in \mathbb{R}^+$ and $T_0 \in \mathbb{R}^+$ are the current temperature (K) and initial temperature (K), respectively; the second term refers to the heat loss in the process of heat convection, heat conduction and heat radiation; $A \in \mathbb{R}^+$ is a surface area (m²) of the quartz lamp tube; $\beta \in \mathbb{R}^+$ is the convective coefficient (W/m²·K) and $\lambda \in \mathbb{R}^+$ is the conductive coefficient (W/m·K); $\varepsilon \in \mathbb{R}^+$ is the blackness and $\sigma \in \mathbb{R}^+$ is the Stephen Boltzmann's constant (W/m²·K⁴); $F \in \mathbb{R}^+$ is an angle coefficient.

2.3. Energy Conservation of the AHGSHV System

According to the law of energy conservation, the AHGSHV system's mathematical model can be given:

$$\frac{U_1^2}{R} \left\{ \frac{\sin[2\alpha(t)]}{2\pi} + \frac{\pi - \alpha(t)}{\pi} \right\} t = cm[T_1(t) - T_0] + A \left\{ \beta[T_1(t) - T_0] + \lambda[T_1(t) - T_0] + \varepsilon\sigma FT_1^4(t)\Delta t \right\} \tag{6}$$

As a consequence, we develop a link between $T_1(t)$ and $\alpha(t)$ as a fundamental mathematical model of the whole AHGSHV system.

by the specification of quartz lamp heaters, which corresponds to χ of (7). Therefore, the complicated AHGSHV system can be replaced by an ultra-local model.

Define $y^*(t)$ as the reference value of output, and $e(t)$ as the tracking error of output, $e(t)$ can be expressed:

$$e(t) = y^*(t) - y(t) \tag{10}$$

Substituting the derivative of (10) to (7), the tracking error equation can be calculated:

$$\frac{de(t)}{dt} = \frac{dy^*}{dt} - G(t) - \chi u(t) \tag{11}$$

3.2. Time Delay Estimation

The estimation of uncertainties and unknown disturbances is the key role of MFC. TDE [39] uses time-delayed signals from system response and control input to estimate the sum of unknown disturbances by introducing a small delay interval. The sum of the unknown disturbances with a real time is approximately estimated. TDE is defined:

$$G(t) \approx \hat{G}(t) = G(t - \nu) = \frac{dy(t - \nu)}{dt} - \chi u(t - \nu) \tag{12}$$

where, $\nu \in \mathbb{R}^+$ is a small delay interval (s), which depends on sampling period of hardware and $\hat{G}(t)$ is the observation value of $G(t)$.

Define the following equation:

$$\tilde{G}(t) = G(t) - \hat{G}(t) \tag{13}$$

where, $\tilde{G}(t)$ is the observation error.

With the TDE observer, (11) can be further expressed:

$$\frac{de(t)}{dt} = \frac{dy^*}{dt} - \hat{G} - \chi u(t) \tag{14}$$

3.3. STNFOSMCTDE

Compared with the traditional integer-order sliding mode controller, STNFOSMC has three advantages. The first one is that fractional order PID has more extra degrees of freedom from integrator and differentiator than integer-order PID. Secondly, the fractional order PID combined with the nonlinear function fal has the characteristics of reducing static error and saturation error and increasing the convergence speed. Thirdly, the super twisting reaching law reduces the high-frequency chattering.

The nonlinear fractional order PID sliding mode surface is designed:

$$s_1(t) = \varphi_{na}fal(e, \gamma, \eta) + \varphi_{nb}D_t^{\phi-1}fal(e, \gamma, \eta) + \varphi_{nc}D_t^\psi fal(e, \gamma, \eta) \tag{15}$$

where

$$fal(e, \gamma, \eta) = \begin{cases} |e(t)|^\gamma \text{sign}[e(t)] & |e(t)| > \eta \\ \frac{e(t)}{\eta^{1-\gamma}} & |e(t)| < \eta \end{cases}$$

$$\text{sign}[e(t)] = \begin{cases} 1 & e(t) > 0 \\ 0 & e(t) = 0 \\ -1 & e(t) < 0 \end{cases}$$

$0 < \gamma < 1, \eta > 0$, and $\varphi_{na}, \varphi_{nb}$, and φ_{nc} are positive coefficients. $\phi > 1, \psi > 0$, and $D_t^{\phi-1}, D_t^\psi$ are fractional integral and fractional derivative, respectively.

In addition, the $fal(e, \gamma, \eta)$ is a piecewise form owing to the existence of $|e(t)| = \eta$; during the sliding mode control, the (15) has the continuity property because the mentioned above TDE is a real-time compensator. When the system state is at the points $|e(t)| = \eta$,

TDE will be a feedforward compensator. The nonlinear term of $fal(e, \gamma, \eta)$ is determined by γ , and the static error can be changed by adjusting the value of γ . The larger $e(t)$ and the smaller gain make the system have minor saturation error. Besides, the another is that the smaller $e(t)$ and the larger gain led to the quick convergence.

The time derivative of $s_1(t)$ can be obtained:

$$\frac{ds_1(t)}{dt} = \begin{cases} \varphi_{na}\gamma|e(t)|^{\gamma-1}\frac{de(t)}{dt} + \varphi_{nb}D_t^\phi fal(e, \gamma, \eta) + \varphi_{nc}D_t^{\psi+1} fal(e, \gamma, \eta) & |e(t)| > \eta \\ \frac{\varphi_{na}}{\eta^{1-\gamma}}\frac{de(t)}{dt} + \varphi_{nb}D_t^\phi fal(e, \gamma, \eta) + \varphi_{nc}D_t^{\psi+1} fal(e, \gamma, \eta) & |e(t)| < \eta \end{cases} \quad (16)$$

where the (15) has the differentiability except the points $|e(t)| = \eta$; because of the (12) as a feedforward compensator, the (16) has the continuity property of its derivative.

Sliding mode surface must meet the requirement of accessibility. In order to ensure that the sliding mode surface can be reached in any initial state, we use the reaching law to ensure accessibility and normal motion phase. Super twisting algorithm combined the reaching law function can reduce the chattering phenomenon which caused by high frequency switching. Super twisting reaching law can be written:

$$\frac{ds_1(t)}{dt} = -\lambda_3|s_1(t)|^{1/2}\text{sign}[s_1(t)] - \lambda_4 \int \text{sign}[s_1(t)]dt + \tilde{g}(t) \quad (17)$$

where $\text{sign}[s_1(t)] = \begin{cases} 1 & s_1(t) > 0 \\ 0 & s_1(t) = 0 \\ -1 & s_1(t) < 0 \end{cases}$, $\lambda_3 > 0$ and $\lambda_4 > 0$ are control rate of super twisting reaching law. $\tilde{g}(t)$ is the perturbation term and is globally bounded, which satisfies

$$\tilde{g}(t) = \begin{cases} \varphi_{na}\gamma|e(t)|^{\gamma-1}\tilde{G}(t) & |e(t)| > \eta \\ \varphi_{na}\frac{1}{\eta^{1-\gamma}}\tilde{G}(t) & |e(t)| < \eta \end{cases} \quad |\tilde{g}(t)| \leq \omega|s_1(t)|^{1/2} \quad (18)$$

where $\omega \in \mathbb{R}$.

Substituting (14) and (17) to (16), $u(t)$ can be calculated:

$$u(t) = \begin{cases} \chi^{-1}\frac{dy^*}{dt} - \chi^{-1}\hat{G} + \frac{1}{\varphi_{na}\gamma|e(t)|^{\gamma-1}\chi} \left\{ \varphi_{nb}D_t^\phi fal(e, \gamma, \eta) + \varphi_{nc}D_t^{\psi+1} fal(e, \gamma, \eta) + \lambda_3|s_1(t)|^{1/2}\text{sign}[s_1(t)] + \lambda_4 \int \text{sign}[s_1(t)]dt \right\} & |e(t)| > \eta \\ \chi^{-1}\frac{dy^*}{dt} - \chi^{-1}\hat{G} + \frac{\eta^{1-\gamma}}{\varphi_{na}\chi} \left\{ \varphi_{nb}D_t^\phi fal(e, \gamma, \eta) + \varphi_{nc}D_t^{\psi+1} fal(e, \gamma, \eta) + \lambda_3|s_1(t)|^{1/2}\text{sign}[s_1(t)] + \lambda_4 \int \text{sign}[s_1(t)]dt \right\} & |e(t)| < \eta \end{cases} \quad (19)$$

3.4. Stability Analysis

In order to ensure that sliding mode surface meets the requirement of stability. The following Lyapunov function [18,30] for the STNFOSMCTDE scheme is defined:

$$V(s) = 2\lambda_4|s_1(t)| + \frac{1}{2}\left(-\lambda_4 \int \text{sign}[s_1(t)]dt\right)^2 + \frac{1}{2}\left(\lambda_3|s_1(t)|^{1/2}\text{sign}[s_1(t)] + \lambda_4 \int \text{sign}[s_1(t)]dt\right)^2 \quad (20)$$

The Lyapunov function can be written as a quadratic form:

$$V(s) = \delta^T J \delta \quad (21)$$

where, $\delta^T = \left[|s_1(t)|^{1/2}\text{sign}[s_1(t)] \quad -\lambda_4 \int \text{sign}[s_1(t)]dt \right]$, $J = \begin{bmatrix} \frac{4\lambda_4+\lambda_3^2}{2} & -\frac{\lambda_3}{2} \\ -\frac{\lambda_3}{2} & 1 \end{bmatrix}$. J is a positive definite matrix and $V(s) > 0$.

To calculate $\dot{V}(s)$, we must calculate $\dot{\delta}^T$. The time derivative of δ^T is:

$$\dot{\delta}^T = \left[\frac{d\{|s_1(t)|^{1/2}\text{sign}[s_1(t)]\}}{dt} \quad -\frac{d\{\lambda_4 \int \text{sign}[s_1(t)]dt\}}{dt} \right] \quad (22)$$

where the first term of (22) is given:

$$\frac{d\left\{|s_1(t)|^{1/2}\text{sign}[s_1(t)]\right\}}{dt} = \frac{1}{2}|s_1(t)\text{sign}[s_1(t)]|^{-1/2}\left\{-\lambda_3|s_1(t)|^{1/2}\text{sign}[s_1(t)] - \lambda_4 \int \text{sign}[s_1(t)]dt + \tilde{\omega}|s_1(t)|^{1/2}\text{sign}[s_1(t)]\right\} \quad (23)$$

where, the second term of (22) is given:

$$-\frac{d\left\{\lambda_4 \int \text{sign}[s_1(t)]dt\right\}}{dt} = -\frac{\lambda_4|s_1(t)|^{1/2}\text{sign}[s_1(t)]}{\left|s_1(t)\right|^{1/2}\text{sign}[s_1(t)]} \quad (24)$$

Then, substituting (23) and (24) to (22), $\dot{\delta}^T$ can be written:

$$\dot{\delta}^T = -\frac{1}{|s_1(t)\text{sign}[s_1(t)]|^{1/2}} * \left[|s_1(t)|^{1/2}\text{sign}[s_1(t)] \quad -\lambda_4 \int \text{sign}[s_1(t)]dt \right] * \begin{bmatrix} \frac{\lambda_3 - \tilde{\omega}}{2} & \lambda_4 \\ -\frac{1}{2} & 0 \end{bmatrix} = -\frac{\delta^T K}{|s_1(t)\text{sign}[s_1(t)]|^{1/2}} \quad (25)$$

where $K = \begin{bmatrix} \frac{\lambda_3 - \tilde{\omega}}{2} & \lambda_4 \\ -\frac{1}{2} & 0 \end{bmatrix}$.

Then, substituting (25), δ^T and J , the time derivative of $V(s)$ is:

$$\dot{V}(s) = 2\delta^T J \delta = -\frac{2\delta^T K J \delta}{|s_1(t)\text{sign}[s_1(t)]|^{1/2}} = -\frac{2\delta^T}{|s_1(t)\text{sign}[s_1(t)]|^{1/2}} \begin{bmatrix} \frac{\lambda_3 - \tilde{\omega}}{2} & \lambda_4 \\ -\frac{1}{2} & 0 \end{bmatrix} * \frac{1}{2} * \begin{bmatrix} 4\lambda_4 + \lambda_3^2 & -\lambda_3 \\ -\lambda_3 & 2 \end{bmatrix} \delta \quad (26)$$

where

$$L = L_1 L_2 = \frac{\lambda_3}{2} \begin{bmatrix} 2\lambda_4 - \frac{\tilde{\omega}(4\lambda_4 + \lambda_3^2)}{\lambda_3} + \lambda_3^2 & -\lambda_3 + \frac{\tilde{\omega}}{2} \\ -\lambda_3 + \frac{\tilde{\omega}}{2} & 1 \end{bmatrix} L_1 = \begin{bmatrix} \frac{\lambda_3 - \tilde{\omega}}{2} & \lambda_4 \\ -\frac{1}{2} & 0 \end{bmatrix} L_2 = \begin{bmatrix} 4\lambda_4 + \lambda_3^2 & -\lambda_3 \\ -\lambda_3 & 2 \end{bmatrix} \quad (27)$$

And L is a positive definite matrix when it satisfies $[\lambda_3(2\lambda_4 + \lambda_3^2)] / (4\lambda_4 + \lambda_3^2) > \tilde{\omega}$, $2\lambda_4 - 4\tilde{\omega}\lambda_4/\lambda_3 - \tilde{\omega}^2/4 > 0$, $\delta^T \delta > 0$, so, $\dot{V}(s) < 0$. Some details of the calculation L are given in the Appendix A.

Using (21), an inequality can be obtained:

$$\epsilon_{\min}\{J\} \|\delta\|_2^2 \leq V(s) \leq \epsilon_{\max}\{J\} \|\delta\|_2^2 \quad (28)$$

$$\|\delta\|_2^2 = \left\{|s_1(t)|^{1/2}\text{sign}[s_1(t)]\right\}^2 + \left\{-\lambda_4 \int \text{sign}[s_1(t)]dt\right\}^2 \quad (29)$$

where $\|\delta\|_2^2$ is the Euclidean norm; $\epsilon_{\min}\{J\}$ and $\epsilon_{\max}\{J\}$ are minimum eigenvalue and maximum eigenvalue of matrix J , respectively.

Using (28), an inequality can be calculated:

$$\epsilon_{\min}^{1/2}\{J\} \|\delta\|_2 \leq V^{1/2}(s) \leq \epsilon_{\max}^{1/2}\{J\} \|\delta\|_2 \quad (30)$$

Using (29) and (30), inequalities can be got:

$$|s(t)|^{1/2} \leq \|\delta\|_2 \leq \frac{V^{1/2}(s)}{\epsilon_{\min}^{1/2}\{J\}} \quad (31)$$

$$-\|\delta\|_2^2 \leq -\frac{V(s)}{\epsilon_{\max}\{J\}} \quad (32)$$

Using (31), an inequality can be got:

$$-1/|s(t)|^{1/2} \leq -\frac{\epsilon_{\min}^{1/2}\{J\}}{V^{1/2}(s)} \quad (33)$$

Using (26), an inequality can be obtained:

$$\dot{V}(s) = -\frac{\delta^T L \delta}{|s_1(t)\text{sign}[s_1(t)]|^{1/2}} \leq -\frac{\zeta_{\min}\{L\}\|\delta\|_2^2}{|s_1(t)\text{sign}[s_1(t)]|^{1/2}} \tag{34}$$

where $\zeta_{\min}\{L\}$ is the minimum eigenvalue of matrix L .

The (34) can be calculated by (32) and (33):

$$\dot{V}(s) \leq -\frac{\zeta_{\min}\{L\}\|\delta\|_2^2}{|s_1(t)\text{sign}[s_1(t)]|^{1/2}} \leq -\frac{\epsilon_{\min}^{1/2}\{J\}\zeta_{\min}\{L\}\|\delta\|_2^2}{V^{1/2}(s)} \leq -\frac{\epsilon_{\min}^{1/2}\{J\}\zeta_{\min}\{L\}V(s)}{V^{1/2}(s)\epsilon_{\max}\{J\}} \tag{35}$$

Let

$$\dot{V}(s) = -\frac{\epsilon_{\min}^{1/2}\{J\}\zeta_{\min}\{L\}V^{1/2}(s)}{\epsilon_{\max}\{J\}} = -\vartheta V^{1/2}(s) \tag{36}$$

where $\vartheta = \epsilon_{\min}^{1/2}\{J\}\zeta_{\min}\{L\}/\epsilon_{\max}\{J\}$; $T = 2V^{1/2}(s_0)/\vartheta$; when the time is after T , the system state can converge to 0 in finite time. Therefore, the stability of the AHGSHV system can be proved. Moreover, the perturbation term $\tilde{g}(t)$ is globally bounded by (18), and δ^T is convergent, so, the observation error $\tilde{G}(t)$ is also bounded, their gains satisfy: $\lambda_4 > \lambda_3(5\omega\lambda_3 + 4\omega^2)/(2\lambda_3 - 4\omega)$ [40].

4. Flow Simulation Results

In this section, Flow Simulation of SolidWorks 2018 is used to simulate heating environment of HV with determined parameters which can obtain the reference output temperature.

The wing of HV is selected as the simulation object. The specific parameters of the wing are as follows: wing root 3550 mm, wingspan 1250 mm, leading edge sweep angle 70°, trailing edge sweep angle 15°, plate thickness 160 mm, leading edge radius 40 mm. The material of the wing is nickel base superalloy GH105. The flight environment is: altitude 20 km, speed 5.5 Mach, angle of attack 10° cruise. Figure 4 is the wing model drawn in Flow Simulation of SolidWorks according to the above parameters. As is shown in Figure 4b, it is a three-dimensional simulation drawing of the model by Flow Simulation. In addition, Figure 4c,d are the sampling points and a fitting curve of surface average temperature, respectively. Figure 4d is used as the reference output value to compare the actual output of the quartz lamp heaters controller. The fitting curve is:

$$y^* = 7.224 * 10^{-6}t^6 - 0.001041t^5 + 0.05614t^4 - 1.353t^3 + 11.86t^2 + 43.25t + 279.2 \tag{37}$$

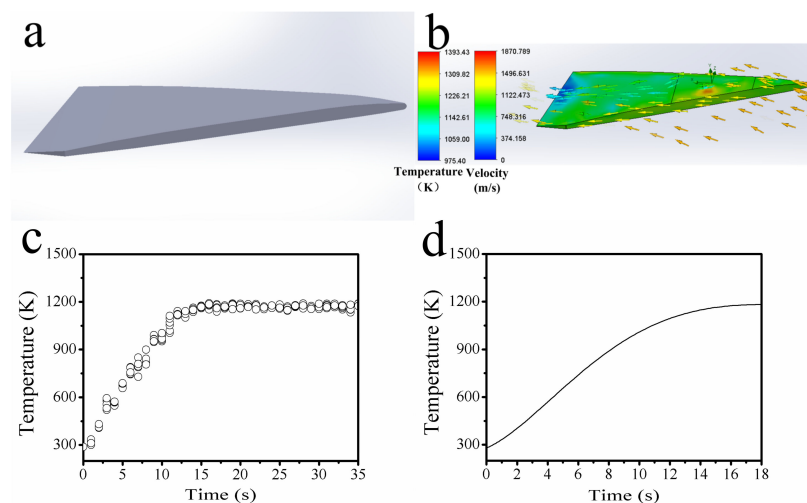


Figure 4. (a) Three-dimensional drawing and (b) flow simulation of the hypersonic vehicle’s wing; (c) sampling points and (d) a fitting curve of surface average temperature.

5. Simulation Results

In order to verify the superiority of STNFOSMCTDE, the simulation is carried out in Matlab Simulink. At the same time, it is compared with LFOSMC, IPID and traditional PID in actual output tracking, error tracking without and with external disturbances.

5.1. LFOSMC Controller

The sliding mode surface of LFOSMC is given:

$$s_0(t) = \varphi_a e(t) + \varphi_b D_t^{\phi-1} e(t) + \varphi_c D_t^\psi e(t) \tag{38}$$

where $\varphi_a > 0, \varphi_b > 0, \varphi_c > 0$, and φ_a, φ_b , and φ_c are the coefficients of proportional, integral and derivative terms of fractional order, respectively, which are used for parameters adjustment; $D_t^{\phi-1}$ and D_t^ψ are the fractional integral and derivative of the sliding mode surface, respectively.

Super twisting reaching law of LFOSMC is written:

$$\dot{s}_0 = -\lambda_1 |s_0(t)|^{1/2} \text{sign}[s_0(t)] - \lambda_2 \int \text{sign}[s_0(t)] dt \tag{39}$$

where λ_1 and λ_2 are control rate of super twisting reaching law.

According to (15), (38) and (39), LFOSMC is designed:

$$u(t) = \chi^{-1} \frac{dy^*}{dt} - \chi^{-1} \hat{G} + \frac{\varphi_b D_t^\phi e(t)}{\varphi_a \chi} + \frac{\varphi_c D_t^{\psi+1} e(t)}{\varphi_a \chi} + \frac{1}{\varphi_a \chi} \left\{ \lambda_1 |s_0(t)|^{1/2} \text{sign}[s_0(t)] + \lambda_2 \int \text{sign}[s_0(t)] dt \right\} \tag{40}$$

5.2. IPID Controller and Traditional PID Controller

The AHGSHV system is closed the loop via the IPID controller which is designed as follows:

$$u(t) = \chi^{-1} \left[-\hat{G} + \frac{dy^*}{dt} + K_p e(t) + K_i \int e(t) dt + K_d \frac{de(t)}{dt} \right] \tag{41}$$

where K_p, K_i and K_d are the coefficients of proportional, integral and derivative terms of IPID.

Traditional PID controller is defined as follows:

$$u(t) = K_{tp} e(t) + K_{ti} \int e(t) dt + K_{td} \frac{de(t)}{dt} \tag{42}$$

where K_{tp}, K_{ti} and K_{td} are the coefficients of proportional, integral and derivative terms of traditional PID.

5.3. Simulation Results Analysis

The specific parameters of the selected quartz lamp heaters are $c = 130 \text{ J/kg}\cdot\text{K}$, $\rho = 1.935 \times 10^4 \text{ kg/m}^3$, $m = 1.46 \times 10^{-2} \text{ kg}$, $A = 2.9 \times 10^{-3} \text{ m}^2$, $\beta = 11.6 \text{ W/m}^2\cdot\text{K}$, $\lambda = 174 \text{ W/m}\cdot\text{K}$, $U_1 = 220 \text{ V}$, $R = 3.08 \text{ }\Omega$, $\varepsilon = 0.97$, $\sigma = 5.67 \times 10^{-8} \text{ W/m}^2\cdot\text{K}^4$, $F = 1$. The parameters of STNFOSMCTDE are $\chi = -100, \nu = 0.03, \varphi_{na} = 5, \varphi_{nb} = 1, \varphi_{nc} = 1, \phi = 0.5, \psi = 120.8, \gamma = 0.4, \eta = 0.3, \lambda_3 = 1000, \lambda_4 = 1$; the parameters of LFOSMC are $\chi = -300, \nu = 0.03, \varphi_a = 1.5, \varphi_b = 0.5, \varphi_c = 110, \phi = 80.5, \psi = 100.3, \lambda_1 = 5000, \lambda_2 = 3000$; the parameters of IPID and PID are $\chi = 500, \nu = 0.03, K_p = -2000, K_i = -10, K_d = -0.1, K_{tp} = -0.05, K_{ti} = -10, K_{td} = -0.006$. All parameters are in Tables 1–5.

Table 1. Parameters of the quartz lamp heaters.

Symbol	Parameter (Unit)	Description
c	130 J/kg·K	specific heat capacity of the quartz lamp filament
ρ	1.935×10^4 kg/m ³	density of the quartz lamp filament
m	1.46×10^{-2} kg	mass of the quartz lamp filament
A	2.9×10^{-3} m ²	surface area of the quartz lamp tube
β	11.6 W/m ² ·K	convective coefficient
λ	174 W/m·K	conductive coefficient
U_I	220 V	voltage of source
R	3.08 Ω	total resistance of the quartz lamp filament
ε	0.97	blackness
σ	5.67×10^{-8} W/m ² ·K ⁴	Stephen Boltzmann’s constant
F	1	angle coefficient

Table 2. Parameters of the STNFOSMCTDE controller.

	ν	φ_{na}	φ_{nb}	φ_{nc}	ϕ
−100	0.03	5	1	1	0.5
ψ	γ	η	λ_3	λ_4	
120.8	0.4	0.3	1000	1	

Table 3. Parameters of the LFOSMC controller.

χ	ν	φ_a	φ_b	φ_c
−300	0.03	1.5	0.5	110
ϕ	ψ	λ_1	λ_2	
80.5	100.3	5000	3000	

Table 4. Parameters of the IPID controller.

χ	ν^*	K_p	K_i	K_d
500	0.03	−2000	−10	−0.1

* The sampling frequency of designed experiment platform is 100 HZ, and in this simulation, three times of sampling period is chosen.

Table 5. Parameters of the traditional PID controller.

K_{tp}	K_{ti}	K_{td}
−0.05	−10	−0.006

As is shown in Figure 5, the tracking temperature trajectory performances have been obtained with four different controllers. These simulation results effectively demonstrate the superiorities of fractional order, nonlinear function *fal*, super twisting reaching law; TDE and an ultra-local model. Figure 5a is a reference temperature trajectory of a hypersonic vehicle’s wing corresponding to Equation (37), which is from 288.15 K to 1180.319 K. As a whole, there is a similar trend of tracking temperature trajectory performances for four different controllers. From the partial enlarged drawing of Figure 5c, STNFOSMCTDE and LFOSMC have fast response and non-overshoot phenomena, whereas IPID and PID have max overshoot because of FOSMC and super twisting reaching law. FOSMC can bring extra degrees of freedom from integrator and differentiator and avoid some contradictions between rapidity and overshoot from PID linear superposition. Moreover, from Figure 5f, the chattering of PID is obvious from 0 s to 0.3 s and that of LFOSMC is very large after 3.0 s, but that of STNFOSMCTDE is very small after 6.0 s, because of the nonlinear function *fal*, which achieves a balance between saturation error and convergent rate.

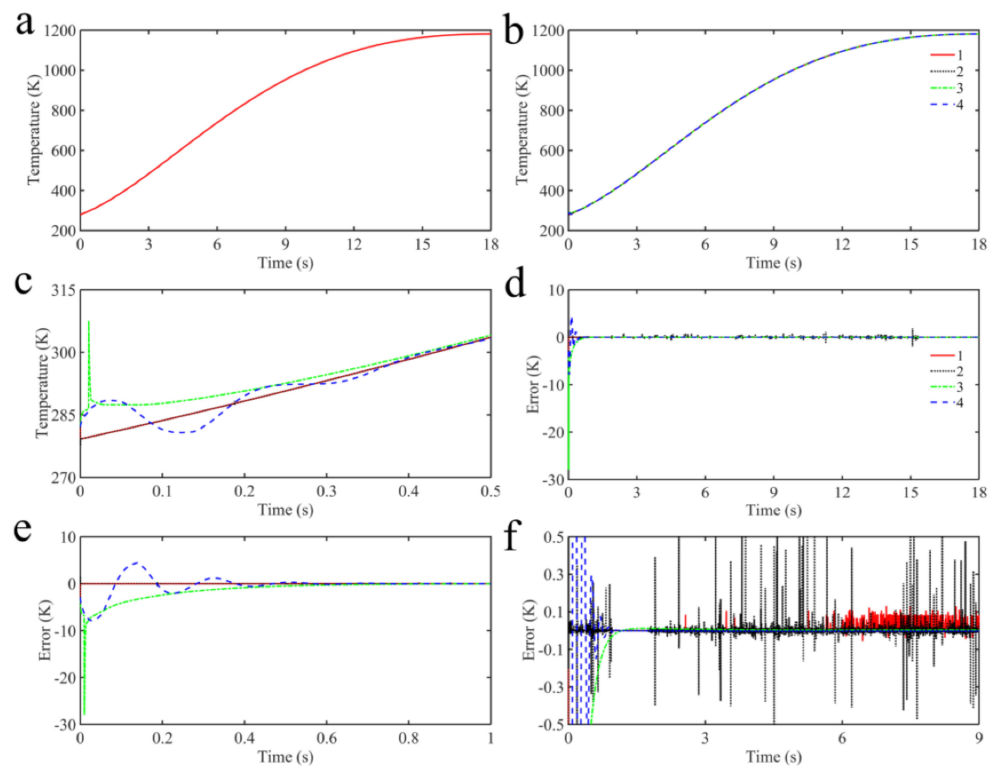


Figure 5. Simulation results without extra disturbances: (a) reference temperature trajectory of a hypersonic vehicle’s wing; (b) tracking temperature trajectory; (c) partial enlarged drawing of tracking temperature trajectory; (d) tracking errors; (e,f) partial enlarged drawings of tracking errors among (1) STNFOSMCTDE, (2) LFOSMC, (3) IPID and (4) PID.

Noting that the resistance of quartz lamp heaters changes with temperature, the variational resistance is taken as the external disturbance. The external disturbance, time-varying resistance, is expressed as:

$$R = 3.08 * (1 + 0.0045y^*) \tag{43}$$

In Figure 6a, there is a line of time-varying resistance respect to time and temperature. From Figure 6f, the chattering of PID is more than 5.0 K from 0 s to 0.4 s, and those of IPID and LFOSMC are obvious after 0.5 s, whereas that of STNFOSMCTDE is the same as before which there is no external disturbances. No matter whether there are external disturbances, STNFOSMCTDE has better rapidity and smaller overshoot. Some reasons are explained: by contrast with PID, IPID has a TDE, as lumped uncertainties estimator, which is integrated into an ultra-local model and TDE plays a role of online compensation; due to adding the nonlinear function *fal*, fast response, strong robustness, and accurate tracking are guaranteed simultaneously along with NFOSMC and super twisting reaching law.

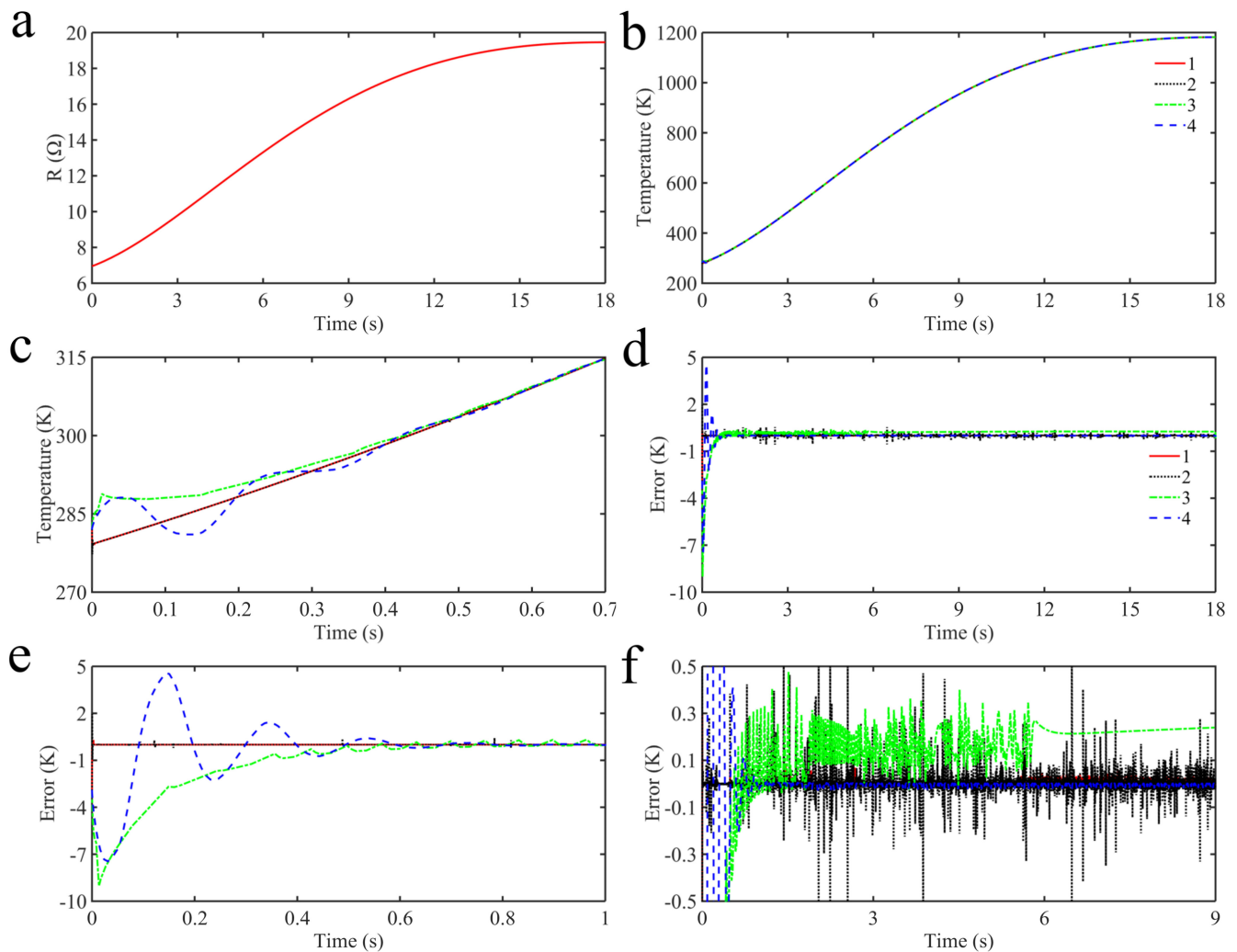


Figure 6. Simulation results with (a) extra disturbances; (b) tracking temperature trajectory; (c) partial enlarged drawing of tracking temperature trajectory; (d) tracking errors; (e,f) partial enlarged drawings of tracking errors among (1) STNFOSMCTDE, (2) LFOSMC, (3) IPID and (4) PID.

Figures 7 and 8 are some simulation results of tracking reference step temperature trajectory without and with external disturbances, respectively. As is shown in Figure 7a, the reference step temperature trajectory is 800 K between 0 s and 10 s and 1200 K after 10 s. The chattering of PID is obvious from 0 s to 0.3 s and from 10 s to 10.3 s, while STNFOSMCTDE, LFOSMC and IPID are almost no chattering. Considering the external disturbance in Figure 8, LFOSMC has the largest overshoot, followed by PID and IPID, while STNFOSMCTDE has no overshoot. The chattering of the LFOSMC is very large and close to 1400 K from 0 s to 0.03 s and 10 s to 10.03 s and that of PID is also obvious from 0 s to 0.2 s and 10 s to 10.2 s. So, the step target can be tracked stably by STNFOSMCTDE.

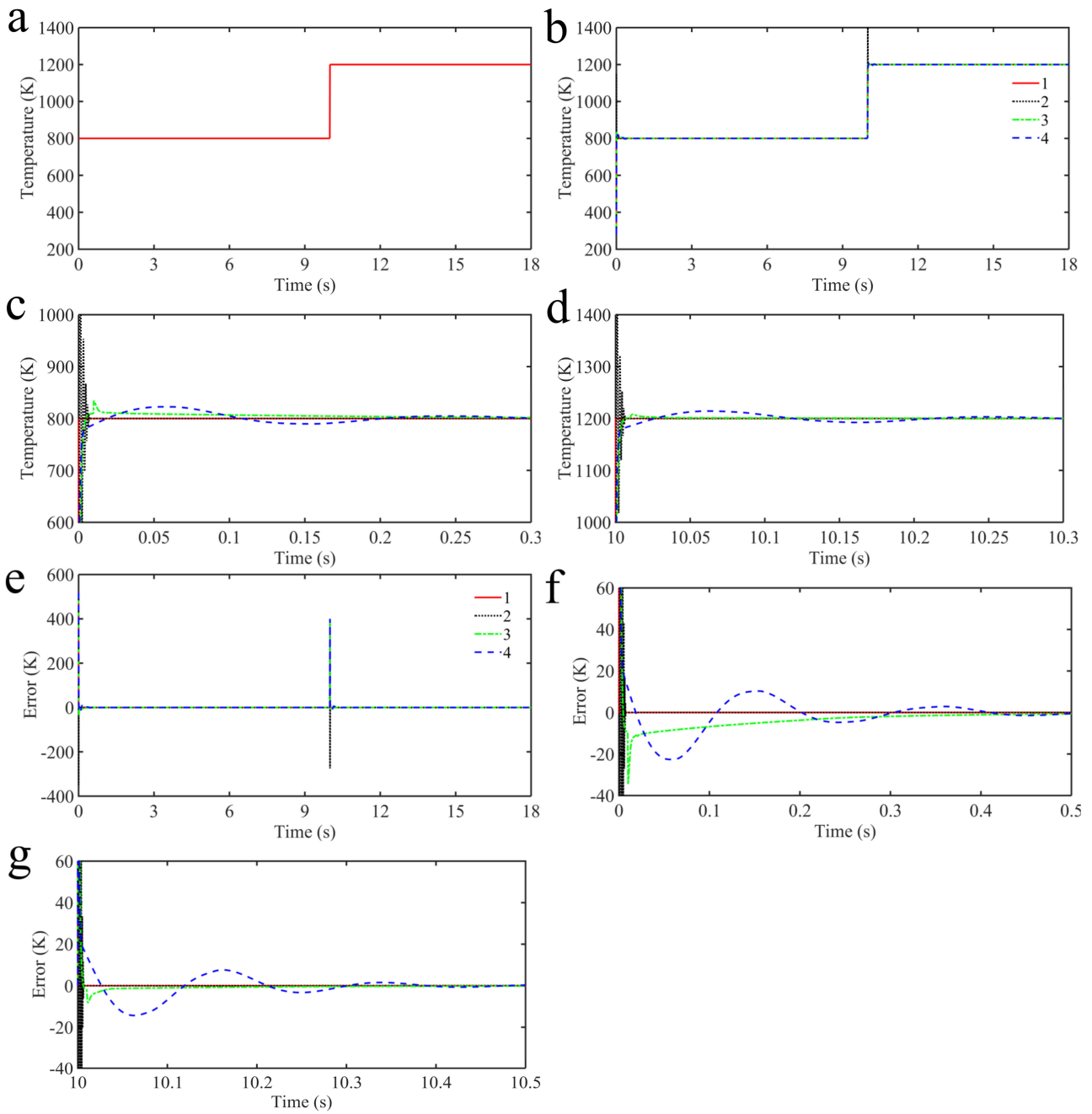


Figure 7. Simulation results without extra disturbances: (a) reference step temperature trajectory; (b) tracking temperature trajectory; (c,d) partial enlarged drawings of tracking temperature trajectory; (e) tracking errors; (f,g) partial enlarged drawings of tracking errors among (1) STNFOSMCTDE, (2) LFOSMC, (3) IPID and (4) PID.

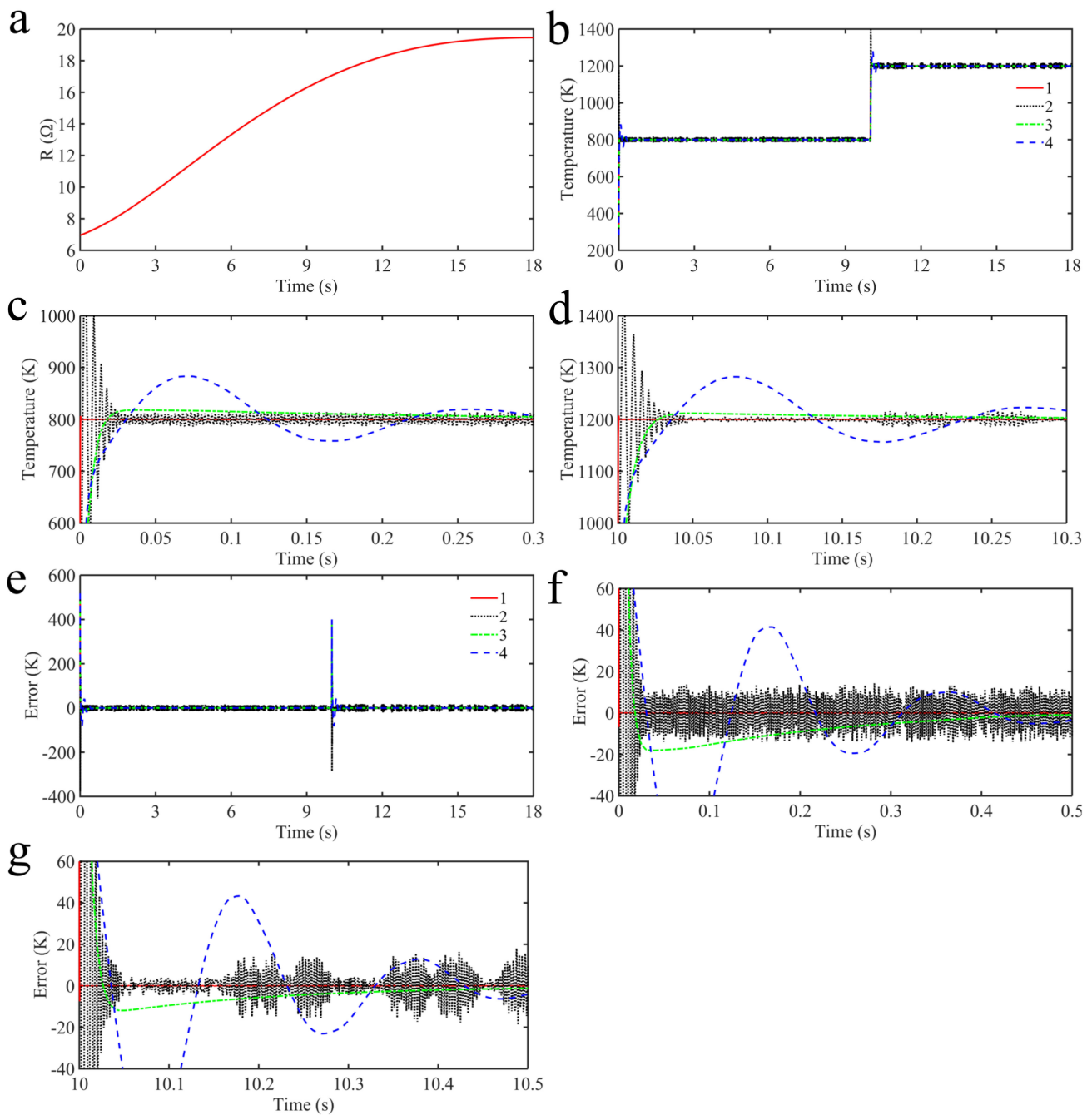


Figure 8. Simulation results with (a) extra disturbances: (b) tracking temperature trajectory; (c) and (d) partial enlarged drawings of tracking temperature trajectory; (e) tracking errors; (f,g) partial enlarged drawings of tracking errors among (1) STNFOSMCTDE, (2) LFOSMC, (3) IPID and (4) PID.

Hence, these simulation results have demonstrated that the STNFOSMCTDE controller is more effective than the other three controllers, because of fractional order, nonlinear function fal , ST reaching law, and TDE. In addition, via model-free control, NFOSMC, super twisting reaching law, and TDE are integrated into an ultra-local model to achieve high tracking precision, fast convergent response, and strong robustness.

In addition, some numerical indicators [18,30] are calculated for quantitative comparison between STNFOSMCTDE and other schemes. These numerical indicators consist of integral absolute error (IAE), average chattering magnitude (ACM), the average deviation of the sliding variables (ADS), and control energy factor (CE). The calculation results are

listed in Table 6. Some details are explained that condition 1 is tracking Figure 5a reference temperature trajectory without external disturbances; condition 2 is tracking Figure 5a reference temperature trajectory with external disturbances; condition 3 is tracking Figure 7a reference step temperature trajectory without external disturbances; condition 4 is tracking Figure 7a reference step temperature trajectory with external disturbances.

Table 6. Numerical indicators for STNFOSMCTDE, LFOSMC, IPID, and PID.

	IAE	ACM	ADS	CE	
STNFOSMCTDE	53.238	0.0259	3.978	424.261	Condition1
LFOSMC	79.631	0.0309	6.523	582.743	
IPID	356.273	1.022		2324.482	
PID	228.397	0.484		3377.336	
STNFOSMCTDE	49.633	0.0752	0.325	374.457	Condition2
LFOSMC	60.723	0.0943	0.669	446.086	
IPID	640.691	0.704		1300.251	
PID	161.903	0.399		2707.088	
STNFOSMCTDE	83.418	0.0529	1.5815	390.284	Condition3
LFOSMC	115.676	0.0824	2.0693	523.026	
IPID	404.183	0.163		948.589	
PID	534.141	0.175		942.382	
STNFOSMCTDE	81.591	0.404	0.966	376.947	Condition4
LFOSMC	114.289	0.609	1.496	573.784	
IPID	509.087	1.013		718.184	
PID	774.194	1.509		1472.41	

Referring to Table 6, STNFOSMCTDE has improved the dynamics performance in comparison with LFOSMC over 33.1%, 15.9%, 39.1%, 27.2% in terms of IAE, ACM, ADS, CE under the condition 1; 18.3%, 20.3%, 51.4%, 16.1% under condition 2; 27.9%, 35.8%, 23.6%, 25.4% under condition 3; 28.6%, 33.7%, 35.4%, 34.3% under condition 4. Accordingly, the numerical indicators validate the superiority of STNFOSMCTDE to LFOSMC, IPID and PID, in terms of control accuracy, convergence rate, and chattering.

6. Conclusions

In this paper, an aerodynamic heating ground simulation for HV, named AHGSHV system, is set on the basis of thermal radiation characteristics of quartz lamp heaters. According to the law of energy conservation, the mathematical model of AHGSHV system is obtained with high nonlinearities and strong couplings from trigonometric functions and high order terms. In order to guarantee satisfactory control performance, fractional order, nonlinear function *fal*, super twisting reaching law, TDE are integrated into an ultra-local model, called STNFOSMCTDE. Thanks to fractional order, it can provide extra degrees of freedom from integrator and differentiator. The nonlinear function *fal*, combined with super twisting reaching law, achieves a balance from saturation error to convergent rate and reduces chattering phenomenon to further improve the rapidity and stability. Moreover, TDE plays a key role of online compensation which can observe uncertain terms and disturbances. Then, the stability of STNFOSMCTDE is proved by Lyapunov stability proof method. Finally, two simulation software, SolidWorks 2018 and MATLAB, are used to verify that some superiorities of STNFOSMCTDE to other controllers in terms of rapidity, overshoot and anti-interference ability. Some numerical indicators validate the effectiveness of STNFOSMCTDE in terms of IAE, ACM, ADS, CE for maximum 33.1%, 35.8%, 51.4%, 34.3%, respectively. In the future, we will pay more attention to AHGSHV system experiments. For some selected HV, thermal protection experiments are ready with STNFOSMCTDE. Moreover, coupled thermal, structural and vibrational analyses should be considered.

Author Contributions: Conceptualization, X.L.; methodology, X.L.; software, M.Z.; validation, M.Z., Z.S. and Z.B.; formal analysis, X.L. and I.V.A.; data curation, X.L.; writing—original draft preparation, X.L.; writing—review and editing, M.Z.; visualization, M.Z.; supervision, I.V.A.; project administration, G.Z.; funding acquisition, G.Z. All authors have read and agreed to the published version of the manuscript.

Funding: This research is funded by China Scholarship Council (No. 202108670007).

Institutional Review Board Statement: Not applicable.

Informed Consent Statement: Not applicable.

Data Availability Statement: Data sharing not applicable.

Acknowledgments: The authors would like to express their gratitude to all those who helped them during the writing of this paper. The authors would like to thank the anonymous for their valuable comments and suggestions.

Conflicts of Interest: The authors declare no conflict of interest.

Appendix A

If $L \in R^{2 \times 2}$ is a positive definite matrix, then it satisfies:

$$2\lambda_4 - \frac{\tilde{\omega}(4\lambda_4 + \lambda_3^2)}{\lambda_3} + \lambda_3^2 > 0 \quad \left| \begin{array}{cc} 2\lambda_4 - \frac{\tilde{\omega}(4\lambda_4 + \lambda_3^2)}{\lambda_3} + \lambda_3^2 & -\lambda_3 + \frac{\tilde{\omega}}{2} \\ -\lambda_3 + \frac{\tilde{\omega}}{2} & 1 \end{array} \right| > 0 \quad (A1)$$

Based on $\lambda_3 > 0$, $\lambda_4 > 0$ and $0 < \tilde{\omega} < \omega$, the (A1) is calculated:

$$\frac{\lambda_3(2\lambda_4 + \lambda_3^2)}{4\lambda_4 + \lambda_3^2} > \tilde{\omega}2\lambda_4 - \frac{4\tilde{\omega}\lambda_4}{\lambda_3} - \frac{\tilde{\omega}^2}{4} > 0 \quad (A2)$$

References

1. Yan, T.; Cai, Y.; Xu, B. Evasion guidance for air-breathing hypersonic vehicles against unknown pursuer dynamics. *Neural Comput. Appl.* **2022**, *34*, 5213–5224. [\[CrossRef\]](#)
2. Simsek, B.; Uslu, S. One-Dimensional Aerodynamic Heating and Ablation Prediction. *J. Aerosp. Eng.* **2019**, *32*, 04019048. [\[CrossRef\]](#)
3. Vinh Tung, L.; Goo, N.S.; Kim, J.Y. Thermomechanical Behavior of Superalloy Thermal Protection System Under Aerodynamic Heating. *J. Spacecr. Rocket.* **2019**, *56*, 1432–1448.
4. Lv, L.; Xiang, Y.; Gu, Z.; Huang, C. Dynamic characteristics of convection heat and radiation heat on building surfaces under cyclic heat flow. *Sci. Prog.* **2022**, *105*, 00368504221075189. [\[CrossRef\]](#) [\[PubMed\]](#)
5. Sinha, R.; Gulhane, N.P. Numerical study of radiation heat loss from solar cavity receiver of parabolic dish collector. *Numer. Heat Transf. Part A-Appl.* **2020**, *77*, 743–759. [\[CrossRef\]](#)
6. Yu, K.; Xu, J.; Liu, S.; Zhang, X. Starting characteristics and phenomenon of a supersonic wind tunnel coupled with inlet model. *Aerosp. Sci. Technol.* **2018**, *77*, 626–637. [\[CrossRef\]](#)
7. Blinova, E.N.; Libman, M.A.; Petrovskij, V.N.; Pimenov, E.V.; Umnov, P.P.; Filippova, V.P.; Chueva, T.R.; Shurygina, N.A. Effect of laser treatment on the strength characteristics of the gamma-phase in alloys of the iron-chromium-nickel system. *Izv. Ross. Akad. Nauk. Seriya Fiz.* **2021**, *85*, 984–989.
8. Remes, Z.; Stuchlik, J.; Stuchlikova, T.-H.; Kupcik, J.; Mortet, V.; Taylor, A.; Ashcheulov, P.; Volodin, V.A. Electroluminescence of thin film p-i-n diodes based on a-SiC:H with integrated Ge nanoparticles star. *Eur. Phys. J. Appl. Phys.* **2020**, *88*, 30302. [\[CrossRef\]](#)
9. Lee, K.H.; Bae, J.S.; Yeum, J.H.; Park, J.; Sung, C.; Kim, J.; Oh, W. Thermal characteristics of epoxy composites with graphite and alumina. *Thermochim. Acta* **2019**, *676*, 115–119. [\[CrossRef\]](#)
10. Potze, W. Radiation heat transfer in axisymmetric quartz glass tubes. *J. Quant. Spectrosc. Radiat. Transf.* **2004**, *84*, 575–586. [\[CrossRef\]](#)
11. Zhu, Y.; Wei, D.; Liu, S.; Zeng, L.; Gui, Y. Power optimization of non-uniform aerodynamic heating simulated by quartz lamp array. *Acta Aeronaut. Et Astronaut. Sin.* **2019**, *40*, 122761.
12. Yu, Y.; Ming, P.; Zhou, S. Numerical Study on Transient Heat Transfer of a Quartz Lamp Heating System. *Math. Probl. Eng.* **2014**, *2014*, 530476. [\[CrossRef\]](#)
13. Wu, D.; Pan, B.; Gao, Z.; Mu, M.; Zhu, L.; Wang, Y. On the Experimental Simulation of Ultra-high Temperature, High Heat Flux and Nonlinear Aerodynamic Heating Environment and Thermo-machanical Testing Technique. *J. Exp. Mech.* **2012**, *27*, 255–271.

14. Lv, X.; Zhang, G.; Zhu, M.; Ouyang, H.; Shi, Z.; Bai, Z.; Alexandrov, I.V. Adaptive Neural Network Global Nonsingular Fast Terminal Sliding Mode Control for a Real Time Ground Simulation of Aerodynamic Heating Produced by Hypersonic Vehicles. *Energies* **2022**, *15*, 3284. [[CrossRef](#)]
15. Hailemichael, A.; Salaken, S.M.; Karimoddini, A.; Homaifar, A.; Khosravi, A.; Nahavandi, S. Developing a computationally effective Interval Type-2 TSK Fuzzy Logic Controller. *J. Intell. Fuzzy Syst.* **2020**, *38*, 1915–1928. [[CrossRef](#)]
16. Huang, C.; Fan, J.M.; Li, W.C.; Chen, X.; Zhu, Q. ReachNN: Reachability Analysis of Neural-Network Controlled Systems. *Acm Trans. Embed. Comput. Syst.* **2019**, *18*, 1–22. [[CrossRef](#)]
17. Bai, W.; Li, T.; Tong, S. NN Reinforcement Learning Adaptive Control for a Class of Nonstrict-Feedback Discrete-Time Systems. *IEEE Trans. Cybern.* **2020**, *50*, 4573–4584. [[CrossRef](#)]
18. Ahmadi, B.; Xie, W.-F.; Zakeri, E. Robust Cascade Vision/Force Control of Industrial Robots Utilizing Continuous Integral Sliding-Mode Control Method. *IEEE-Asme Trans. Mechatron.* **2022**, *27*, 524–536. [[CrossRef](#)]
19. Gao, P.; Zhang, G.; Lv, X. Model-Free Hybrid Control with Intelligent Proportional Integral and Super-Twisting Sliding Mode Control of PMSM Drives. *Electronics* **2020**, *9*, 1427. [[CrossRef](#)]
20. Li, S.; Wang, H.; Tian, Y.; Aitouch, A.; Klein, J. Direct power control of DFIG wind turbine systems based on an intelligent proportional-integral sliding mode control. *ISA Trans.* **2016**, *64*, 431–439. [[CrossRef](#)]
21. Zhang, X.; Wang, H.; Tian, Y.; Peyrodie, L.; Wang, X. Model-free based neural network control with time-delay estimation for lower extremity exoskeleton. *Neurocomputing* **2018**, *272*, 178–188. [[CrossRef](#)]
22. Wang, H.; Ye, X.; Tian, Y.; Zheng, G.; Christov, N. Model-Free-Based Terminal SMC of Quadrotor Attitude and Position. *IEEE Trans. Aerosp. Electron. Syst.* **2016**, *52*, 2519–2528. [[CrossRef](#)]
23. Guo, B.; Chen, Y.; Zhou, A. Event trigger-based adaptive sliding mode fault-tolerant control for dynamic systems. *Sci. China-Inf. Sci.* **2021**, *64*, 1–3. [[CrossRef](#)]
24. Do, T.D. Disturbance Observer-Based Fuzzy SMC of WECSs Without Wind Speed Measurement. *IEEE Access* **2017**, *5*, 147–155. [[CrossRef](#)]
25. Ling, J.; Feng, Z.; Zheng, D.; Yang, J.; Yu, H.; Xiao, X. Robust adaptive motion tracking of piezoelectric actuated stages using online neural-network-based sliding mode control. *Mech. Syst. Signal Processing* **2021**, *150*, 107235. [[CrossRef](#)]
26. Kamal, S.; Sharma, R.K.; Thach Ngoc, D.; Ms, H.; Bandyopadhyay, B. Sliding mode control of uncertain fractional-order systems: A reaching phase free approach. *Asian J. Control* **2021**, *23*, 199–208. [[CrossRef](#)]
27. Zhang, B.; Pi, Y.; Luo, Y. Fractional order sliding-mode control based on parameters auto-tuning for velocity control of permanent magnet synchronous motor. *ISA Trans.* **2012**, *51*, 649–656. [[CrossRef](#)] [[PubMed](#)]
28. Gao, P.; Zhang, G.M.; Ouyang, H.M.; Mei, L. An Adaptive Super Twisting Nonlinear Fractional Order PID Sliding Mode Control of Permanent Magnet Synchronous Motor Speed Regulation System Based on Extended State Observer. *IEEE Access* **2020**, *8*, 53498–53510. [[CrossRef](#)]
29. Wang, Y.; Chen, J.; Yan, F.; Zhu, K.; Chen, B. Adaptive super-twisting fractional-order nonsingular terminal sliding mode control of cable-driven manipulators. *ISA Trans.* **2019**, *86*, 163–180. [[CrossRef](#)] [[PubMed](#)]
30. Zakeri, E.; Moezi, S.A.; Eghtesad, M. Optimal interval type-2 fuzzy fractional order super twisting algorithm: A second order sliding mode controller for fully-actuated and under-actuated nonlinear systems. *ISA Trans.* **2019**, *85*, 13–32. [[CrossRef](#)]
31. Sheng, Y.Z.; Bai, W.J.; Xie, Y.W. Fractional-order (PID)-D-lambda sliding mode control for hypersonic vehicles with neural network disturbance compensator. *Nonlinear Dyn.* **2021**, *103*, 849–863. [[CrossRef](#)]
32. Song, J.; Wang, L.; Cai, C.; Qi, X. Nonlinear fractional order proportion-integral-derivative active disturbance rejection control method design for hypersonic vehicle attitude control. *Acta Astronaut.* **2015**, *111*, 160–169. [[CrossRef](#)]
33. Zhang, Y.; Niu, H.; Chai, T. Data-based un-modeled dynamics driven nonlinear PID. *Control Theory Appl.* **2020**, *37*, 481–491.
34. Han, J. From PID to Active Disturbance Rejection Control. *IEEE Trans. Ind. Electron.* **2009**, *56*, 900–906. [[CrossRef](#)]
35. Rawat, A.; Jha, S.K.; Kumar, B.; Mohan, V. Nonlinear fractional order PID controller for tracking maximum power in photo-voltaic system. *J. Intell. Fuzzy Syst.* **2020**, *38*, 6703–6713. [[CrossRef](#)]
36. Haghghi, D.A.; Mobayen, S. Design of an adaptive super-twisting decoupled terminal sliding mode control scheme for a class of fourth-order systems. *ISA Trans.* **2018**, *75*, 216–225. [[CrossRef](#)]
37. Lee, J.; Chang, P.H.; Jin, M. Adaptive Integral Sliding Mode Control With Time-Delay Estimation for Robot Manipulators. *IEEE Trans. Ind. Electron.* **2017**, *64*, 6796–6804. [[CrossRef](#)]
38. Xia, L.; Qi, B.; Tian, N. Study on Modeling Analysis and Testing Method of Electro-thermal Properties of Quartz Lamp. *Infrared Technol.* **2015**, *37*, 877–882.
39. Youceftoumi, K.; Ito, O. A time-delay controller for systems with unknown dynamics. *J. Dyn. Syst. Meas. Control -Trans. Asme* **1990**, *112*, 133–142. [[CrossRef](#)]
40. Moreno, J.A.; Osorio, M.A. A Lyapunov approach to second-order sliding mode controllers and observers. In Proceedings of the 2008 47th IEEE Conference on Decision and Control, Cancún, Mexico, 9–11 December 2008.